

Hot Carrier Thermalization and Josephson Inductance Thermometry in a Graphene-based Microwave Circuit

Raj Katti,^{1,*} Harpreet Arora,^{2,3,*} Olli-Pentti Saira,^{1,4,*} Kenji Watanabe,⁵ Takashi Taniguchi,⁵ Keith C. Schwab,^{1,2} Michael Roukes,^{1,2} and Stevan Nadj-Perge^{2,3,†}

¹*Department of Physics, California Institute of Technology, Pasadena, California 91125, USA*

²*T. J. Watson Laboratory of Applied Physics, California Institute of Technology, 1200 East California Boulevard, Pasadena, California 91125, USA*

³*Institute for Quantum Information and Matter, California Institute of Technology, Pasadena, California 91125, USA*

⁴*Brookhaven National Laboratory, Upton NY 11973, USA*

⁵*National Institute for Materials Science, Namiki 1-1, Tsukuba, Ibaraki 305 0044, Japan*

Due to its exceptional electronic and thermal properties, graphene is a key material for bolometry, calorimetry, and photon detection. However, despite graphene's relatively simple electronic structure, the physical processes responsible for the transport of heat from the electrons to the lattice are experimentally still elusive. Here, we measure the thermal response of low-disorder graphene encapsulated in hexagonal boron nitride (hBN) by integrating it within a multi-terminal superconducting device coupled to a microwave resonator. This technique allows us to simultaneously apply Joule heat power to the graphene flake while performing calibrated readout of the electron temperature. We probe the thermalization rates of both electrons and holes with high precision and observe a thermalization scaling exponent consistent with cooling dominated by resonant electron-phonon coupling processes occurring at the interface between graphene and superconducting leads. The technique utilized here is applicable for wide range of semiconducting-superconducting interface heterostructures and provides new insights into the thermalization pathways essential for the next-generation thermal detectors.

Graphene provides a tantalizing opportunity for the design and development of bolometric detectors, due to its exceedingly small heat capacity [1, 2], much smaller compared to traditionally synthesized thin films. In addition, the thermal conductivity of graphene can be greatly changed by coupling it to superconducting or normal electrodes or placing it on different substrates. Moreover, when graphene is contacted using superconducting electrodes, the resulting Josephson coupling and the corresponding supercurrents are highly dependent on electron temperature [3]. Accordingly, graphene-based Josephson junctions (gJJs) are particularly promising for detecting ultra-small thermal responses at milli-Kelvin temperatures. In turn, gJJs can be tuned in many ways, as graphene couples well with a variety of superconductors to form highly transparent junctions, enabling supercurrents to persist over several microns [4, 5]. Using different superconductors, junction geometry, and operation at different carrier densities allows, in principle, for a range of specific optimizations needed for detecting small heat and optical signals. To achieve the highest sensitivity, for example, one can choose to operate at the lowest temperatures and employ superconductors with a small superconducting gap, similar to the approach that is taken in conventional superconducting nanowire-based detectors. If a large dynamic range is required, tuning the critical currents in graphene junctions by controlling carrier density can provide additional flexibility in design.

Despite the significant progress in integrating graphene with superconducting nanoelectronic devices, the present understanding of the thermalization of electrons and holes in these systems is still incomplete. In most transport measurements performed to date, thermalization in gJJs is thought to be primarily driven by the electron-phonon interaction in graphene bulk [7], as the diffusion of unpaired electrons into the metallic leads is suppressed due to the superconducting gap. However, in the case where graphene is encapsulated within boron nitride (hBN), deduced values of electron-phonon coupling from the experimental thermalization rates [8] are typically orders-of-magnitude larger than theoretical predictions. Such a discrepancy is not expected for materials with a simple band structure such as graphene, where both the electronic and phonon spectrum can be readily calculated. Further, recent scanning SQUID experiments, which provide spatially resolved thermal imaging of graphene [9] have revealed that, when electronic transport in graphene is ballistic, signatures of electron thermalization are present only near physical edges, local defects, and close to metallic contacts. However, such signatures of such boundary-mediated thermalization have not so far been evident in transport measurements. Here we present thermal measurements of a device architecture in which graphene temperature is measured via changes in Josephson inductance [10] caused by heating. In contrast to typical critical current measurements that involve switching between superconducting and resistive states, this approach allows to continuously monitor thermal response with high precision that, in principle, depends only on the measurement integration time. Surprisingly, for both electron and hole doping,

* These authors contributed equally to this work.

† Correspondence: s.nadj-perge@caltech.edu

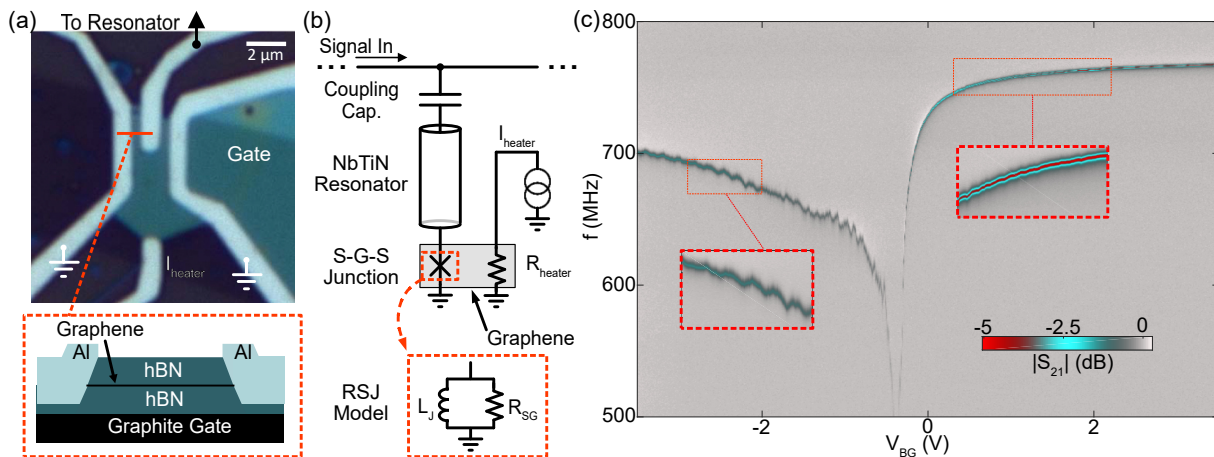


FIG. 1. Graphene Josephson junction and the characterization of the resonator circuit. (a), Optical image showing a top-down view of the graphene flake encapsulated in hexagonal boron nitride (blue-green) contacted by superconducting electrodes (light blue). The top contact is placed in close proximity to the ground wires to form the graphene Josephson junction (gJJ). The bottom contact placed far from the ground electrodes is used to apply Joule heating. The Inset shows the partial cross-section across the gJJ. Tuning the global carrier density in the graphene flake is achieved by applying a DC voltage V_{BG} to a graphite backgate. (b), Simplified electrical circuit schematic (for full schematic see Appendix B). A superconducting Niobium Titanium Nitride (NbTiN) resonator is coupled to the external microwave line via a coupling capacitor and terminated by the gJJ. The gJJ is electrically modeled as the parallel sum of a dissipationless branch of inductance $L_J = \frac{\Phi_0}{2\pi I_c}$ and a dissipative branch of resistance R_{SG} . A dedicated heater port allows application of Joule heat to the graphene flake. (c), $|S_{21}|$ vs. V_{BG} shows the evolution of the resonance feature. Near the charge neutrality point (CNP; $V_{CNP} = -0.3$ V), the gJJ maximally loads the resonator and, consequently, minimizes the resonant frequency. Far from the CNP, the gJJ acts as a low-impedance termination and maximizes the resonant frequency. On the hole-side ($V_{BG} < V_{CNP}$), Fabry-Perot type oscillations are visible due to formation of the regions of different doping in the bulk graphene (hole doping; p-type) and in vicinity of contacts (electron doping; n-type) [6].

we observe temperature dependence of the thermal conductance consistent with a resonant electronic scattering mechanism [11, 12] that occurs at the interface between graphene and superconducting leads.

Figure 1 shows a schematic of the device architecture and basic characterization measurements. A gJJ is integrated into a graphene flake of approximate area $A = 25 \mu\text{m}^2$ (Fig. 1(a)). The gJJ consists of a central superconducting contact separated from two symmetrically placed superconducting contacts shorted to the ground plane. Connection is made at the other end of the flake to a heater port used for thermal characterization (see Appendix A and B for details of device fabrication and the measurement architecture). Superconducting aluminum is used for all contacts as it has a small gap relative to other elemental superconductors; we expect this will maximize temperature sensitivity in the sub-Kelvin temperature range of our measurements. To probe the response of the gJJ supercurrent to changes in electron density and temperature, we couple it to an on-chip resonator [6, 13] (Fig. 1(b)). Since the gJJ acts as an additional inductive element, it modifies the resonant frequency, which we monitor through microwave reflectometry. The parameters characterizing the gJJ, the Josephson inductance $L_J = \frac{\Phi_0}{2\pi I_c}$ and subgap resistance R_{SG} , depend strongly on electron density (see also Ap-

pendix E). Accordingly, the resonant frequency and spectral width are both highly dependent on the back gate voltage V_{BG} [6] (Fig. 1(c)). Note that we can resolve the resonance over a large range of gate voltages; this allows us to study phenomena arising from electron and hole doping as well as near charge neutrality ($V_{BG} \approx -0.4$ V). For hole doping ($V_{BG} < -0.4$ V), Fabry-Perot-type oscillations indicate that carrier transport is ballistic in our high-quality graphene sample.

In addition to the electrostatic doping, the circuit resonance is also strongly dependent upon temperature (Fig. 2). When the device temperature increases, the resonance dip shifts to lower frequencies and broadens, reflecting increased losses occurring within the junction. Importantly, the observed shape of the resonance can be fitted using a standard four-parameter Lorentzian fit function at all accessible carrier densities (2.2×10^{12} holes/cm² $< n_{carrier} < 5.5 \times 10^{11}$ electrons/cm²) and temperatures ($160\text{mK} < T_{max} < 480\text{mK}$) (see also Appendix C). The high level of agreement between data and the fit (Fig. 2(a)) allows us to relate the deduced resonance parameters to the physical properties of the junction. In particular, shifts of resonant frequency f_0 and the overall resonance shape, which is set by internal quality factor Q_i , can be related to parameters of the resistively-shunted junction (RSJ) junction model

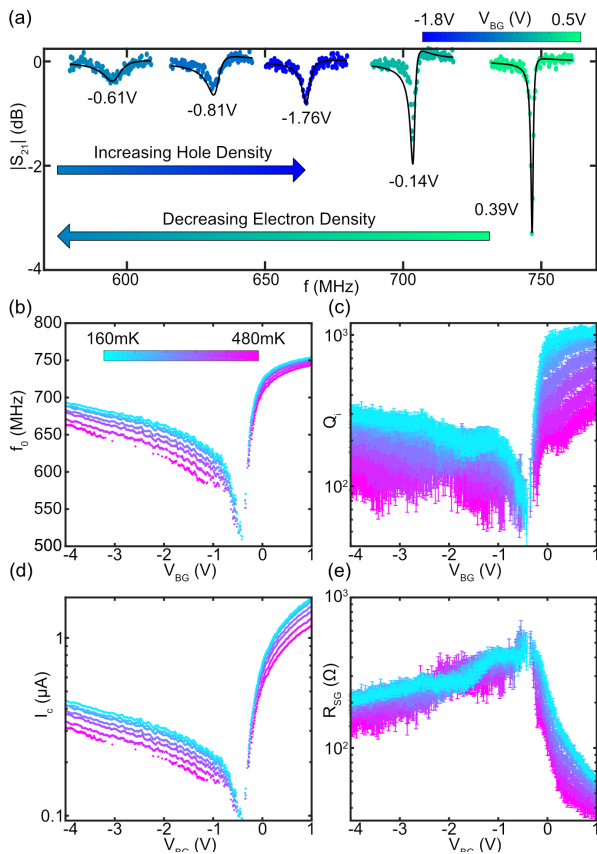


FIG. 2. Resonance Fits and Extracted Parameters. (a), Representative $|S_{21}|$ data and fits for electron and hole doping. Color and labels denote backgate voltage V_{BG} . Arrows show the direction of resonant frequency shifts as V_{BG} is swept from positive voltage (electron doped) to negative voltage (hole doped) through charge-neutrality. Green arrow shows the resonant frequency approaching 500 MHz as electron-doping decreases to charge neutrality. Blue arrow shows that the resonant frequency increasing away from 500 MHz as hole-doping increases. (b), f_0 as a function of V_{BG} for representative $T_{mxc} = 160, 210, 260, 310, 360, 410, 460$ mK. Extracted resonant frequency f_0 as a function of V_{BG} shows a characteristic lineshape consistent with Fig. 1(c). As T_{mxc} increases, f_0 decreases for all backgate voltages. (c), Q_i as a function of V_{BG} and T_{mxc} . (d, e), RSJ model parameters I_c (d), and R_{SG} (e) as a function of V_{BG} and T_{mxc} . I_c and R_{SG} are determined using a numerical impedance model of the resonator/gJJ device with resonance parameters (f_0 , Q_i) as inputs (see Fig. 7).

[14], the gJJ critical current I_c and sub-gap resistance R_{SG} [6] (see Fig. 1(b) and Appendix E). These quantities determine the small-signal electrical response of the junction at any temperature and doping level. We note that an estimate of microwave losses in the junction is not accessible from the switching current measurements that have typically been employed in gJJ threshold detection schemes. Fitting the temperature dependence of $I_c(T)$ allows estimation of an induced superconducting gap $\Delta \sim 80 \mu\text{eV}$ (see Appendix F). Finally, since we ex-

pect the resonator ringdown time τ to be the limiting time constant in our device, we estimate from the fitted resonance parameters that $\tau < 150$ ns for all backgate voltages (see Fig. 7).

To characterize the thermal properties of the gJJ device, we employ a measurement configuration in which the gJJ is heated internally by applying a DC current I_{heater} to the heater port (Fig. 3). The port electrode is placed sufficiently far from the ground electrodes to preclude supercurrent flow. This configuration allows us to accurately monitor the input power delivered to the graphene flake while simultaneously monitoring the resonance frequency. For different device temperatures and doping, representative changes in the S_{21} resonance dip are shown in Fig. 3(a-c) and Fig. 3(f-h). By increasing the stage temperature from 170 mK to 400 mK, we observe a decrease in the resonant frequency of 27 MHz for holes, compared to 6 MHz for electrons. This is consistent with greater inductive loading (lower I_c) in the hole regime (see Appendix E). By applying a heater current I_{heater} , the internal flake temperature T is increased above T_{mxc} , decreasing the resonant frequency. Combined with the measurements taken at different temperatures for calibration (Fig. 3(e,j)) the power vs. temperature characterization and, consequently, the thermal conductivity G_{th} of the graphene flake can be determined. We use this approach to investigate thermal properties for both electron and hole doping regimes.

The data we have acquired is consistent with a power law $P_{heater} = \Sigma A(T^n - T_{mxc}^n)$, with electron temperature T , stage temperature T_{mxc} , scaling exponent n and the electron-phonon coupling prefactor ΣA (see also Appendix G). We plot $\partial P/\partial T = G_{th} = n\Sigma A T^{n-1}$ (Fig. 4(c)) which shows that the scaling exponents for hole and electron doping are consistent with $n = 5$. We note that our fitting procedures produce only comparably small errors for each of the individual data points and, accordingly, the uncertainty of the extracted scaling exponent is much less than 1. This enables us to clearly distinguish that the exponent obtained here is *not* consistent with the $n = 3$ or $n = 4$ scaling predicted for bulk electron-phonon coupling in reduced dimensions [15, 16]. While an $n = 5$ scaling exponent is expected for the electron-phonon coupling of a 3D electron gas [17], these considerations do not apply for our graphene device in which the electron and phonon density-of-states are 2D. Also, we note that the mechanism where hot electrons (or holes) diffuse into the superconducting aluminum leads before thermalization, while in principle possible, is not consistent with our observations (see Appendix H for more detailed discussion).

Measurements of hBN-encapsulated graphene performed previously [5, 8] reveal that G_{th} (scaled by the area) is about three orders-of-magnitude larger than predictions by simple bulk electron-phonon coupling theory. The magnitude of $G_{th} \sim 5 - 300$ pW/K in our measurements is consistent with these observations. Due to enhanced mobility, hBN-encapsulated graphene is typi-

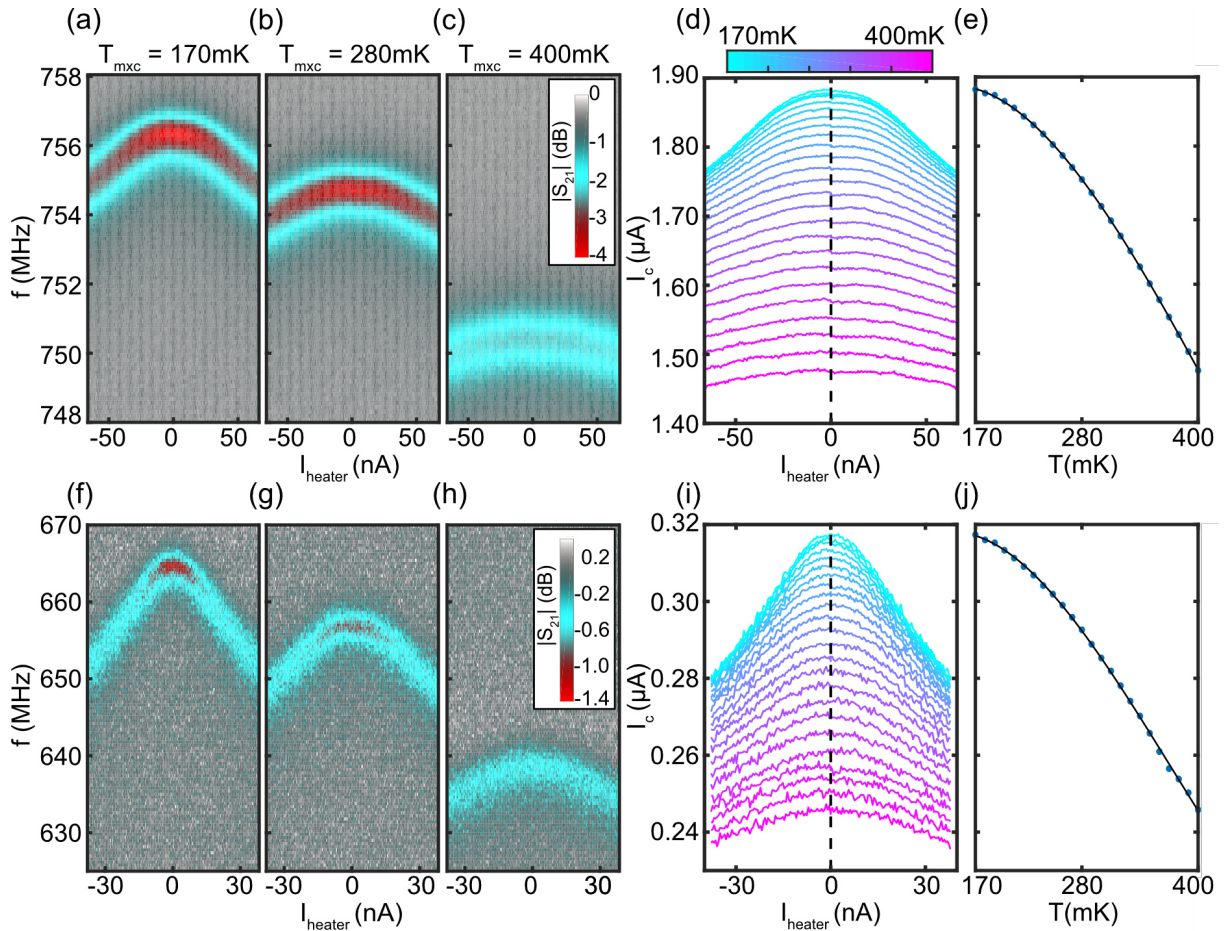


FIG. 3. Electron-side and Hole-side Heating and Calibration. (a-c), Electron-side ($V_{BG} = 1.1$ V) and (f-h) hole-side ($V_{BG} = -1.8$ V) $|S_{21}(f)|$ vs. I_{heater} for three representative mixing stage temperatures (a, f) $T_{mixc} = 170$ mK (b, g) $T_{mixc} = 280$ mK (c, h) $T_{mixc} = 400$ mK. Applying a DC heater current I_{heater} to the designated heater port decreases the resonant frequency of the device. As expected, the shifts are symmetric with respect to the polarity of I_{heater} . (d), Electron-side and (i) hole-side I_c as a function of I_{heater} for different mixing chamber temperatures. Fitting (a-c) and (f-h) allows extraction of resonance parameters (f_0 , Q_i) and junction parameters (I_c , R_{SG}) (see also Appendix D). The dashed line at $I_{heater} = 0$ nA corresponds to the data cut plotted in (e) and (j). (e) Electron-side and (j), hole-side calibration curve, the unheated I_c as a function of T_{mixc} . Since I_c monotonically decreases with increasing mixing chamber temperature T_{mixc} , there is a one-to-one correspondence between I_c and graphene flake temperature.

cally in the ballistic scattering limit, in which the carrier mean free path l_{mfp} is limited by the device dimension ($L_{device} \approx 5 \mu\text{m}$ in our sample). This observation has led to the hypothesis that the enhanced G_{th} may arise from “resonant supercollisions” [11, 12] a scenario consistent with the spatially resolved measurements [9, 18]. In this scenario, defects located at edge of the graphene flake locally enhance electron-phonon interactions and open a thermalization pathway that dominates over electron-phonon coupling in the bulk. Spatially-resolved scanning SQUID measurements show an enhancement of surface phonon temperature at graphene edges and close to metal contacts. Theory formulated to explain these results [12] suggests that an $n = 5$ scaling exponent should

hold down to milli-Kelvin temperatures ($T < T_{BG}$) in the limit of strong scattering ($\delta \sim 1$). In this context, our high precision measurements provide the first clear evidence that an $n = 5$ scaling exponent signaling that resonance supercollisions indeed dominate the thermalization in graphene at sub-Kelvin temperatures. We note that further exploration of the device parameter space (e.g. sample size, aspect ratio, disorder) maybe needed to disentangle relations between different microscopic thermalization mechanisms in general.

We note that G_{th} exhibits a power law consistent with $n = 5$ for both electron and hole doping, indicating that this mechanism remains dominant in both regimes. Interestingly, the electron- and hole-side prefactors differ

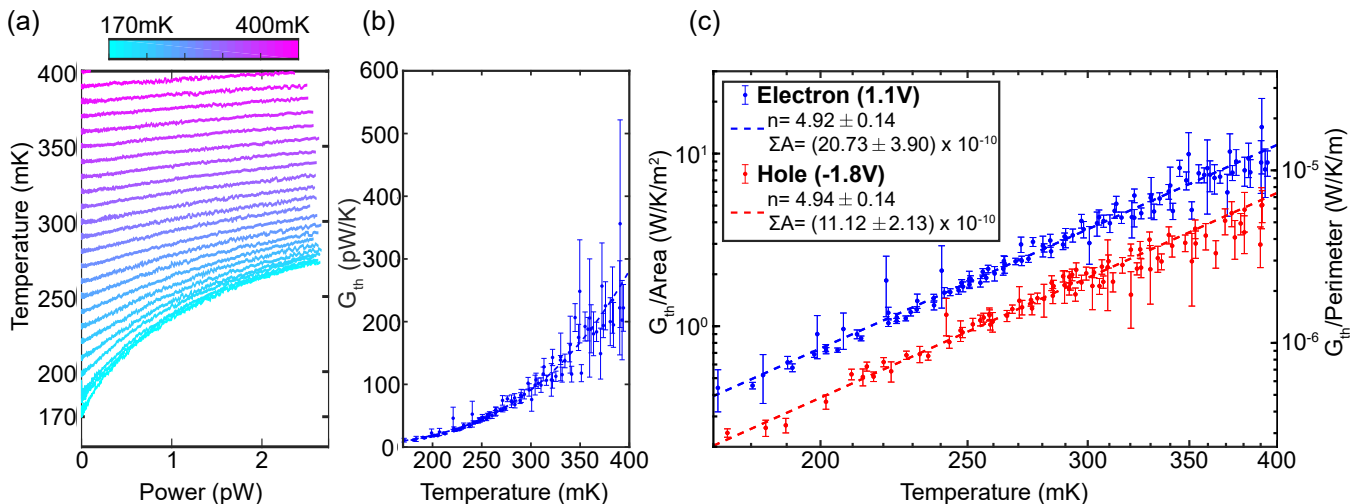


FIG. 4. Power-Temperature Curves. (a) Electron-side flake temperature as a function of heat power. From the injected DC current I_{heater} and measured voltage drop V across the heater port, the injected heater power can be determined $P_{heater} = I_{heater} \times V$. From the I_c vs. I_{heater} traces in Fig. 3(d,i) and the I_c vs. T_{mxc} calibration in Fig. 3(e,j), flake temperature can be determined as a function of applied P_{heater} . Color corresponds to the mixing chamber stage temperature. (b) G_{th} vs. T_{mxc} . Taking the numerical derivative $\frac{\partial P}{\partial T}$ of Fig. 4(a) allows the data to be plotted on a single line. Fit line is to the power law $G_{th} = \partial P / \partial T = n \Sigma A T^{n-1}$ where n is the scaling exponent and ΣA (in units of W/K⁵) is the multiplicative factor. (c) Electron and hole G_{th} vs. T_{mxc} (log-log scale). Hole and electron doping both show power law scaling with an $n = 5$ exponent.

by a factor of approximately two (see Fig. 4(c)). A possible explanation for this difference arises from the energy distribution of resonant scattering centers [9]. In this scenario, different scattering centers are activated when the chemical potential of the flake is shifted by the back-gate. Therefore, it is possible that the difference in the prefactors can be attributed to different populations of activated scatterers. Additionally, we note that, in the case of hole doping, the intrinsic p-n junction formed between the graphene region close to the Al contacts (which is always intrinsically n-doped) and the p-doped bulk may also play a role. In this regime, holes from the bulk must pass across the p-n junction in order to efficiently thermalize via resonant scattering centers. Since the p-n junction has a finite transmission probability, it may therefore reduce the overall thermalization rate. We note that attaining an accurate calculation of the thermalization prefactor from first principles is difficult due to effects outlined above and further theoretical work is needed for quantitative comparisons.

In the context of detector technologies, graphene is argued to be a promising platform for future scalable far-infrared or microwave detector-arrays [8, 19]. Its utility for this purpose is typically evaluated on the basis of optimization of several key attributes including response time, responsivity, thermal insulation and multiplexing that, in turn, require simultaneous optimization of multiple device parameters. The hBN-encapsulated graphene devices studied here provide large supercurrents and sub-microsecond response times that allow for continuous monitoring of thermal response, and integra-

tion of the resonator readout that permits straightforward frequency-division multiplexing of many devices on a single feedline [20, 21]. Moreover, in our scheme the presence of a separate heater port can be employed for broad-spectrum energy detection. We note that a thermal insulation of the architecture employed here can be achieved at the expense of lowering the mobility in graphene by, for example, placing it directly on the oxide substrate [19] instead of hBN.

Finally, we briefly compare the inductance readout scheme employed here with graphene detectors based on junction switching [8, 22] (between the zero and finite voltage state) as their potential applications may significantly differ. The latter type of detectors register a “count” when the incident photon energy is above a given threshold, and therefore forfeit the possibility of energy spectroscopy provided by the linear, resonantly-coupled graphene detector architecture pursued in this work. Further, threshold detectors intrinsically provide slower response, which is limited by the cooling and resetting of the junction after a photon absorption event. While this type of detector may be a desirable option in the experiments where photon energy and arriving time is known or controlled, the inductance readout detection scheme is more suitable for novel spectroscopy applications of unknown sources [23], including dark matter detection [24–27] and photon and phonon counting [28] where linear response and ability to fully evaluate detection performance is important (see Appendix I for noise equivalent power characterization).

Acknowledgments: We acknowledge useful discussions

with Sophie Li, Matt Matheney, Ewa Rej, and Jonas Zmuidzinas. **Funding:** This work was supported by NSF through program CAREER DMR-1753306 and Gist-Caltech memorandum of understanding. S.N.-P. also acknowledges the support of DOE-QIS program (DE-SC0019166), IQIM (NSF funded physics frontiers center) and the Sloan foundation. M.L.R acknowledges support from NSF grant NSF-DMR-1806473.

APPENDIX A: Fabrication

Fabrication of the superconducting resonator and coupling capacitor proceeds by sputtering a few hundred nanometers of Niobium Titanium Nitride (NbTiN) on an undoped silicon wafer with 300 nanometers of thermal oxide. Typical superconducting transition temperatures are ~ 14 K. Subsequently, the resonator and coupling capacitor are patterned by electron beam lithography followed by an SF₆ wet etch and Ar reactive ion etch. The graphene heterostructure is assembled using standard exfoliation and stamping methods and dropped on the resonator chip. 1-D edge contacts between the superconducting metal and graphene heterostructure are patterned by electron beam lithography followed by an Ar reactive ion etch and an electron beam evaporation of the titanium adhesion layer and aluminum contacts.

APPENDIX B: S_{21} Measurement Circuit

A standard S_{21} transmission measurement is performed in which a swept microwave tone is sent out of Port 1 of a PicoVNA 2 vector network analyzer (VNA) and down through attenuators and stages of the dilution refrigerator. The impedance of the resonator/gJJ device loads the line and scatters the incoming microwave tone. The transmitted portion of the microwave signal is amplified by a first-stage $T_n = 4$ K CIT low noise amplifier, and then by three room temperature amplifiers, where it is detected by Port 2 of the VNA.

To improve DC isolation between the device and the VNA, we include inner/outer DC blocks on the ports of the VNA. To vary readout power incident upon to the device, we vary the room temperature attenuation between -50 dB and -80 dB. The attenuation at the fridge stages ensures the 300 K noise at room temperature is attenuated below the noise floor of the mixing chamber. In the diagram, the attenuators and amplifiers are positioned immediately under the fridge stage to which they are thermally anchored.

The heater measurements in Fig. 3 and Fig. 4 of the main text are performed by applying a DC heater current I_{heater} to the heater port of the graphene flake and reading out the corresponding voltage drop in a 4-wire measurement. To source I_{heater} , an Agilent 33210A AWG outputs a DC voltage for the DC heating measurements of the main text and an AC voltage for the noise equi-

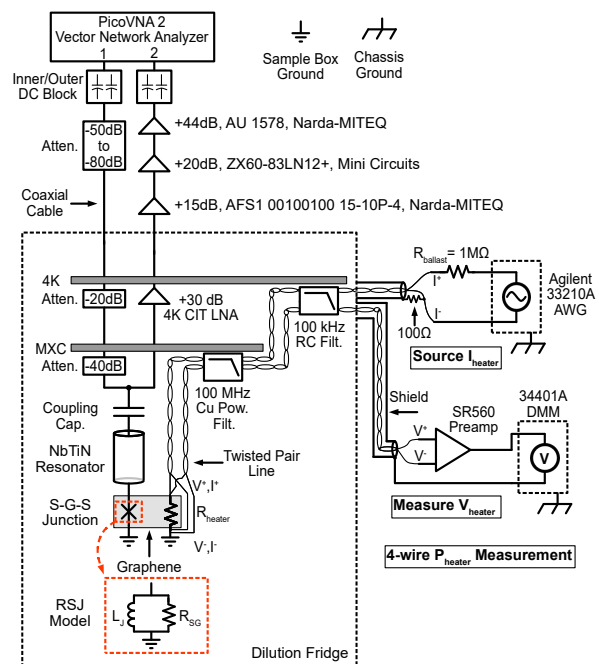


FIG. 5. S_{21} Circuit Diagram. The circuit diagram shows both the S_{21} readout of the resonance feature and the application and readout of P_{heater} . In the S_{21} measurement, a signal is sourced from the PicoVNA2 vector network analyzer (VNA) and passes through a series of attenuators down to the resonator/graphene device held at T_{mix} . The transmitted portion of the signal is amplified by an amplification chain with a first-stage 4K LNA and read out by the VNA. Application of P_{heater} proceeds by sourcing a current I generated by a voltage sourced by the Agilent 33210A AWG and dropped over a 1 M Ω ballast resistor. After passing through a two stages of filters, the sourced current flows through the normal resistance R_{heater} of the heater port of the graphene sample and dissipates Joule heat power in the flake. The voltage drop V across graphene heater is amplified by an SR560 preamp and read out by a 33201A digital multimeter (DMM). In this way, the $P_{heater} = I \times V$ delivered to the graphene flake is measured in a 4-wire measurement.

alent power [29] measurements of section I. Since the ballast resistor $R_{ballast} = 1$ M Ω is 3 orders-of-magnitude larger than the heater port resistance $R_{heater} \approx 1$ k Ω , the series combination of the AWG and $R_{ballast}$ can be well-approximated as a current source I_{heater} . The I_{heater} current travels down PhBr twisted-pair lines to the heater port where it Joule heats the graphene flake. Outside of the fridge, the shield on the twisted pair lines is held at fridge ground. The return line of the twisted pair is grounded through a 100 Ω resistor to a breakout box (not shown) which is also held at fridge ground. The return line terminates at the negative terminal of the AWG. We note that the possible ground loop introduced by the grounding of the twisted pair return line through the 100 Ω resistor does not have an appreciable effect on the measurement.

APPENDIX C: S_{21} Fitting Procedure

Fitting of the resonance feature follows the procedure in Ref. 30. Background-subtracted S_{21} transmission data is fit to a four-parameter fitting function

$$S_{21} = 1 - \frac{Q_0/Q_c - 2iQ_0 \frac{\delta\omega}{\omega_0}}{1 + 2iQ_0 \frac{\omega - \omega_0}{\omega_0}}$$

Extracted fit parameters include resonant frequency ω_0 , internal quality factor Q_i , coupling quality factor Q_c , and asymmetry parameter $\delta\omega_0$. Total quality factor is defined as the parallel sum of the dissipation channels $\frac{1}{Q_0} = \frac{1}{Q_i} + \frac{1}{Q_c}$. Error bars in Fig. 2b-d correspond to the 95% (2σ) confidence level calculated from the covariance matrix of the fits. An asymmetry in the resonance circle can cause the diameter of the resonance circle to occur off of the real axis. Such an asymmetry may arise from a non-negligible line inductance or mismatched input/output impedance.

1. Resonance Dependence on V_{BG}

Figure 1(c) shows how the resonance changes as a function of V_{BG} . The maximal tuning of resonance frequency f_0 with V_{BG} occurs in the range $[V_{CNP}, V_{CNP} + 0.3 \text{ V}]$, where the $\frac{\partial f_0}{\partial V_{BG}} \approx \frac{670 \text{ MHz}}{1 \text{ V}}$. Assuming a parallel-plate capacitance of hBN ($\epsilon_r = 3$) and a separation $d = 30 \text{ nm}$ between the graphene flake and backgate, $\frac{\partial f_0}{\partial n_{\text{carrier}}} \approx \frac{1.21 \text{ GHz}}{10^{12} / \text{cm}^2}$. Since we estimate the area of our graphene flake to be $A = 25 \mu\text{m}^2$, the maximum sensitivity of our device used as an electrometer is $\frac{\partial f_0}{\partial N_{\text{carrier}}} = \frac{4.84 \text{ kHz}}{1 \text{ e}^-}$.

APPENDIX D: Fitting Procedure for Extraction of RSJ Parameters

To deduce the physical parameters of the gJJ from the fit parameters of the S_{21} resonance feature, we employ an electrical impedance model of our device which takes the inputs (f_0 , Q_i) and numerically solves for junction parameters (I_c , R_{SG}). *Sonnet*[®]15.53 is used to estimate the physical parameters of the NbTiN transmission line resonator [31] (See Table I). The coupling capacitance C_c is estimated by fitting a set of resonances at $V_{BG} = -1.9 \text{ V}$, numerically solving for C_c , and creating a histogram of extracted C_c values with mode $C_c = 0.243 \text{ pF}$ and standard deviation of approximately $\sigma_{C_c} = 0.02 \text{ pF}$.

APPENDIX E: Discussion of Extracted Parameters from Resonance Fits and RSJ Model

As shown in Fig. 7, our fitting and modeling procedure allows several fit and junction parameters to be plotted as

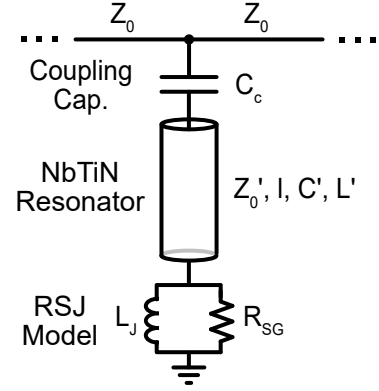


FIG. 6. Impedance Model. The electrical impedance model of the resonator-graphene device consists of the graphene Josephson junction in the RSJ model, a NbTiN transmission line resonator characterized by parameters in Table I, a coupling capacitor C_c , and 50Ω microwave ports.

a function of backgate voltage V_{BG} and flake temperature T_{mxc} .

Figure 7(a) shows a dip in Q_i at $V_{BG} = -2 \text{ V}$, which is propagated to the other plots Fig. 7(b-d). This dip arises from an asymmetry in the S_{21} parameter which rotates the resonance circle off the real axis. Such rotations can arise from line impedance mismatches and parasitic couplings [30]. Since R_{SG} is determined primarily by Q_i , R_{SG} is sensitive to dissipation in the graphene flake as well as the electromagnetic environment of the flake/resonator assembly. By contrast, f_0 and I_c are largely insensitive to these effects, so our thermometry based upon the dispersive shifts of the resonance is also largely insensitive to these effects.

Figure 7(b) shows that our device for all backgate voltages is in the undercoupled limit ($Q_i < Q_c$), where dissipation occurs primarily within device instead of via the coupling to the microwave lines. The variation of the coupling quality factor Q_c is consistent with the circuit model and a constant coupling capacitor $C_c = 0.243 \text{ pF}$.

The dispersive shifts of the resonance can be understood from the impedance model shown in Fig. 6, which consists of a transmission line resonator terminated by the junction impedance. This model predicts an unloaded ($L_J = 0 \text{ nH}$) resonant frequency of $f_{\text{unload}} = 774.75 \text{ MHz}$ as indicated by the solid red line in Fig. 7(f). When a finite inductance L_J loads the transmission line resonator, the resonant frequency decreases. This occurs because a change in the terminating impedance alters the boundary condition at the terminating end of the resonator. In the case of the unloaded resonator, i.e. a $\lambda/4$ resonator, the termination is a short-to-ground, which fixes the boundary voltage at $V = 0$. This enforces the resonance condition that the length of the resonator equals one quarter of the resonant wavelength,

C_C	Coupling capacitor	0.243 pF
l	TLR length	4989 μm
C'	TLR capacitance per length	3515 pF/m
L'	TLR inductance per length	1130 nH/m
Z'_0	TLR characteristic impedance	17.9 Ω
v_{ph}	TLR phase velocity	1.575×10^7 m/s
Z_0	Reference characteristic impedance	50 Ω
Z_{out}	Parallel two-port impedance	25 Ω

TABLE I. Coupling Capacitor, Transmission Line Resonator (TLR), and Microwave Port Parameters.

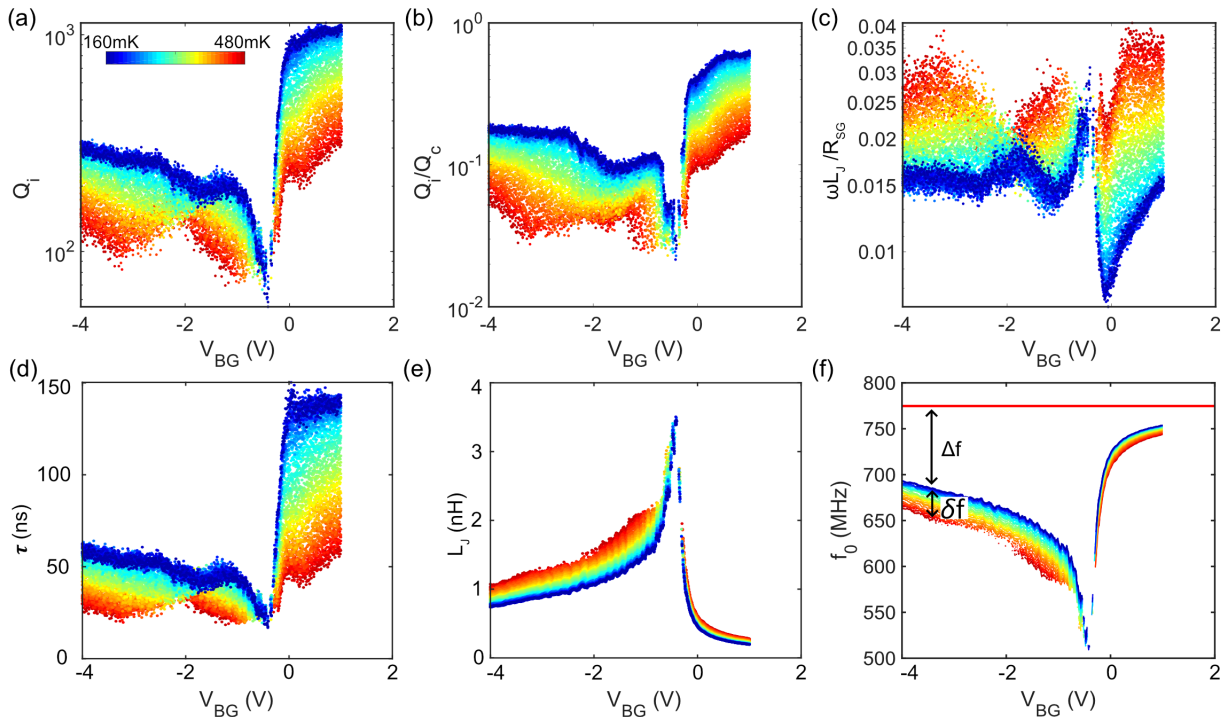


FIG. 7. Extracted Parameters from Resonance Fits and Impedance Model. (a) Q_i vs. V_{BG} . The internal quality factor Q_i is extracted from the S_{21} fit function in C. (b) Q_i/Q_c vs. V_{BG} . Ratio of internal quality factor Q_i and coupling quality factor Q_c (also extracted from the S_{21} fit function) shows that the device is in the undercoupled limit for all backgate voltages. (c) $\omega L_J/R_{SG}$ vs. V_{BG} . Ratio of the inductive branch impedance to resistive branch impedance in the RSJ model. (d) $\tau = Q_0/\omega_i$ vs. V_{BG} . The resonator time constant τ is expected to set the system time constant for all measured backgate voltages and temperatures. (e) L_J vs. V_{BG} . The Josephson inductance $L_J = \frac{\Phi_0}{2\pi I_c}$. (f) f_0 vs. V_{BG} . The red line corresponds to the projected unloaded ($L_J = 0$ nH) resonance frequency. Δf corresponds to the loaded ($L_J \neq 0$ nH) resonance frequency at $T_{mxc} = 160$ mK. δf corresponds to further shift in the resonance frequency due to the increase in flake temperature.

i.e. $\lambda/4 = l$. However, terminating the transmission line resonator in an inductance alters the boundary condition such that the boundary voltage amplitude is fixed at some $V = V_0 > 0$. This has the effect of enforcing the resonance condition that a quarter-wavelength is larger than the resonator length, i.e. $\lambda/4 > l$, or, analogously, that the resonant frequency is decreased relative to the un-

loaded case. The larger the terminating impedance, i.e. the larger L_J , the lower the resonant frequency [6, 31].

Due to higher contact transparency, electron doping should exhibit a larger supercurrent than hole doping. It follows that the electron side should exhibit a smaller L_J than the hole side, and, correspondingly, the electron side should exhibit a smaller decrease in resonant

frequency relative to f_{unload} than the hole side. This is consistent with Fig. 7(f) for electron and hole doping, i.e. $\Delta f_{electron} < \Delta f_{hole}$ where Δf is defined as the resonant frequency decrease at $T_{mxc} = 160$ mK.

Increasing the flake temperature further increases L_J and decreases the resonant frequency. A rough estimate of the further decrease of the resonant frequency δf due to increased temperature is as follows:

$$\frac{|\delta f|}{|\Delta f|} \approx \frac{|\delta I_c|}{|\Delta I_c|}$$

As discussed in the section F, I_c typically decreases by 20-30% as the flake temperature is increased from 160 mK to 400 mK. From the main text Fig. 3,

Hole Side:

$$\frac{|\delta f_{hole}|}{|\Delta f_{hole}|} = \frac{26 \text{ MHz}}{110 \text{ MHz}} \approx 24\%$$

Electron Side:

$$\frac{|\delta f_{electron}|}{|\Delta f_{electron}|} = \frac{5.9 \text{ MHz}}{18.6 \text{ MHz}} \approx 32\%$$

The change in resonant frequency is therefore consistent with the typical change in $I_c(T)$. We conclude that the greater magnitude of frequency decrease on the hole side relative to the electron side follows as a straightforward result of the greater inductive loading of the transmission line resonator.

As shown in Fig. 7(c), $\frac{\omega_0 L_J}{R_{SG}}$ is a common figure-of-merit for RF-driven Josephson junctions [32]. It compares the impedance of the dissipationless supercurrent branch to the dissipative resistive branch. A smaller value of $\frac{\omega_0 L_J}{R_{SG}}$ denotes a less dissipative device. At $T_{mxc} = 160$ mK, $\frac{\omega_0 L_J}{R_{SG}} \approx 1.5\%$ within a factor of 2. As the temperature rises to $T_{mxc} = 400$ mK, $\frac{\omega_0 L_J}{R_{SG}}$ increases to 3%. This is consistent with decreases in I_c raising the impedance of the dissipationless branch and driving more current through the dissipative branch, as indicated by the degrading quality factor with increasing flake temperature (see Fig. 2(c)).

APPENDIX F: I_c vs. T_{mxc} Fits and Extraction of Induced Superconducting Gap

Due to the measurement architecture employed here, we cannot perform 4-wire measurements directly on the gJJ to estimate the induced superconducting gap Δ_0 . Instead, we perform a fitting procedure based upon the temperature dependence of the critical current $I_c(T)$.

The $I_c(T)$ vs. V_{BG} data in Fig. 2(d) is fit to extract physical parameters. The fit function we employ describes the supercurrent that arises from thermally populating the Andreev bound states (ABS) in a ballistic

junction [33].

$$I_c(T) = I_c(0) \tanh\left(\frac{\Delta}{2k_B T}\right)$$

The two fit parameters correspond to the physical parameters $I_c(0)$, the zero-temperature critical current, and Δ , the induced superconducting gap. An example fit is shown in Fig. 8(a).

In Fig. 8(b), modulation of the fit parameter $I_c(0)$ with V_{BG} on the hole side is consistent with *pnp*-type Fabry-Perot interference as discussed in the main text and Fig. 1(c). Following the standard method for determining Fabry-Perot cavity length in ballistic graphene, we subtract the slowly varying background with a fit to a 7th-order polynomial (see Fig. 8(d-e)) and take the power spectral density (see Fig. 8(f)). The large peak in the power spectral density is consistent with a Fabry-Perot cavity length of $L_{cav} = 361.51$ nm. Structure on the electron side could be caused by an *nn'*-type Fabry-Perot cavity [34].

From Fig. 8(c), we can make a coarse estimate of the induced superconducting gap $\Delta \approx 80 \mu\text{V}$. However, further measurements are needed to determine whether the finer structure of Fig. 8(c) is due to the physics of the S-G-S junction or an artifact of the fitting procedure. Toward this end, it would be useful to perform simultaneous RF characterization and DC multiple-Andreev reflection measurements on a gJJ sample [6].

APPENDIX G: Power vs. Temperature Fitting Procedure

To obtain the $G_{th} = \frac{\partial P}{\partial T}$ vs. T in Fig. 4(c), we first perform piece-wise linear fits of the $P-T$ curves of Fig. 4(a). Subsequently, we perform a nonlinear least squares fit of the G_{th} vs. T to the fitting function

$$G_{th} = n\Sigma A T^{n-1} \quad (\text{G1})$$

with free fit parameters n the scaling exponent and ΣA the electron-phonon coupling. The errors in the free fit parameters correspond to the 2σ (95%) errors obtained from the nonlinear least squares fit. On the electron side, we include an exclusion criteria at the limit of the temperature resolution of our device. This criteria does not appreciably change the extracted n or ΣA . Without the exclusion criteria the extracted fit parameters are $n = 5.04 \pm 0.2$ and $\Sigma A = (25.25 \pm 6.89) \times 10^{-10} \text{ W/K}^5$. With the exclusion criteria, the extracted fit parameters are $n = 4.92 \pm 0.14$ and $\Sigma A = (20.73 \pm 3.90) \times 10^{-10} \text{ W/K}^5$.

APPENDIX H: Other thermalization pathways

In this section, we briefly discuss alternative thermalization pathways that can occur in our experimental ge-

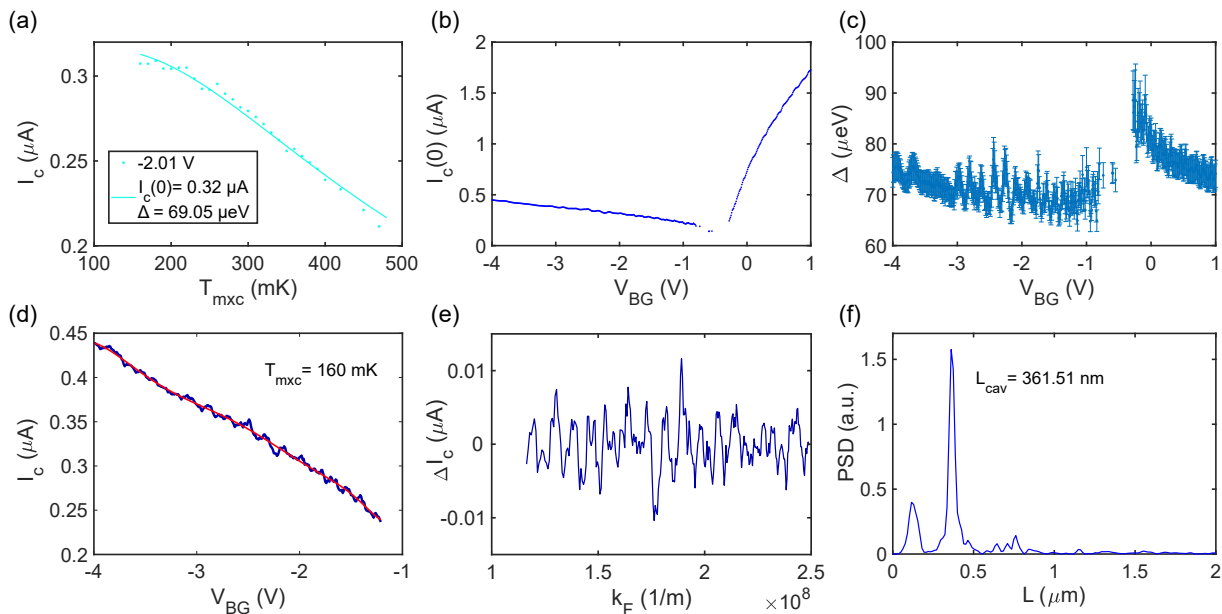


FIG. 8. (a) I_c vs. T . An example fit of I_c vs. T for $V_{BG} = -2.01$ V with extracted fit parameters $I_c(0)$ and Δ . (b) Fit parameter $I_c(0)$ vs. V_{BG} . $I_c(0)$ fit parameter is shown for both electron and hole doping. (c) Fit parameter Δ vs. V_{BG} . A coarse estimate of induced gap $\Delta \approx 80 \mu\text{eV}$. Fine features are discussed in the text. (d) Hole side I_c vs. V_{BG} . Blue trace is hole side I_c data for $T_{mxc} = 160$ mK. Red trace is the slowly-varying background as fit to a 7th-order polynomial. (e) Background-subtracted ΔI_c vs. k_F . ΔI_c is obtained by subtracting the two traces in Fig. 8(d). (f) Power spectral density of ΔI_c . The large peak is consistent with an effective Fabry-Perot cavity length of $L_{cav} = 361.51$ nm.

ometry. While they indeed occur, we note that the thermal conductance corresponding to these alternative pathways are all too small to explain our measurements.

Thermalization via bulk phonons

The bulk phonons are often invoked as the main source of electron thermalization in graphene. However, besides having a different exponent ($n = 3$ or $n = 4$ not agreeing with our data, see Fig. 10), the cooling rate via bulk graphene phonons is too small to explain experimental findings. As discussed in previous literature, the typical thermal conductance expected from bulk phonons is two orders of magnitude smaller than the measured data. We note that, in this context of the overall cooling rate, our measurements are roughly in line with previous graphene-hBN experiments.

Thermalization in Aluminum leads: Another possibility is that the hot electrons enter Al leads. While the tunneling of electrons (or holes) in a superconductor is expected to be suppressed due to the existence of a finite single-particle gap, previous work found that this process can still be sizable when using Aluminum electrodes. The critical distinction between our study and previous work using Aluminum contacts (see, for example, Ref. [35]), is that we used Al only as immediate contact to graphene (Fig. 11), and beyond that, the electrodes used in our experiment are made from Niobium Titanium Nitride (NbTiN) which has a much larger superconducting gap ($\Delta \approx 1$ meV). In this context, the amount of heat that could “leak” into Aluminum contacts

is much lower compared to measured values of thermal conductance. A total volume of Aluminum in our device is only approximately $V = 150 \times 10^{-18}$ m³. By considering the established value for electron-phonon coupling in Aluminum ($\Sigma = 0.3 \times 10^9$ W/K⁵m³, see Ref. [36]) the corresponding P. vs T dependence is expected to follow $P \approx 0.98 \times \Sigma \times V \times T^5 \times \exp(-\Delta/(kT))$. Here $\Delta \approx 170 - 200$ μeV is Aluminum superconducting gap measured in our experiments and a numerical pre-factor of 0.98 is estimated in Ref. [37]. At $T = 200$ mK this rate corresponds to $G = dP/dT = 0.25 \times 10^{-12}$ W, approximately two orders of magnitude smaller than the observed thermalization rates at our lowest temperatures.

APPENDIX I: Noise Equivalent Power

1. Theory

A key figure-of-merit for linear power detectors is noise-equivalent power (*NEP*). A power-to-voltage detector has a responsivity \mathcal{R} , such that

$$V_{out} = \mathcal{R}(P_{in})$$

In the linear-response regime, i.e. for small applied power, this expression simplifies to

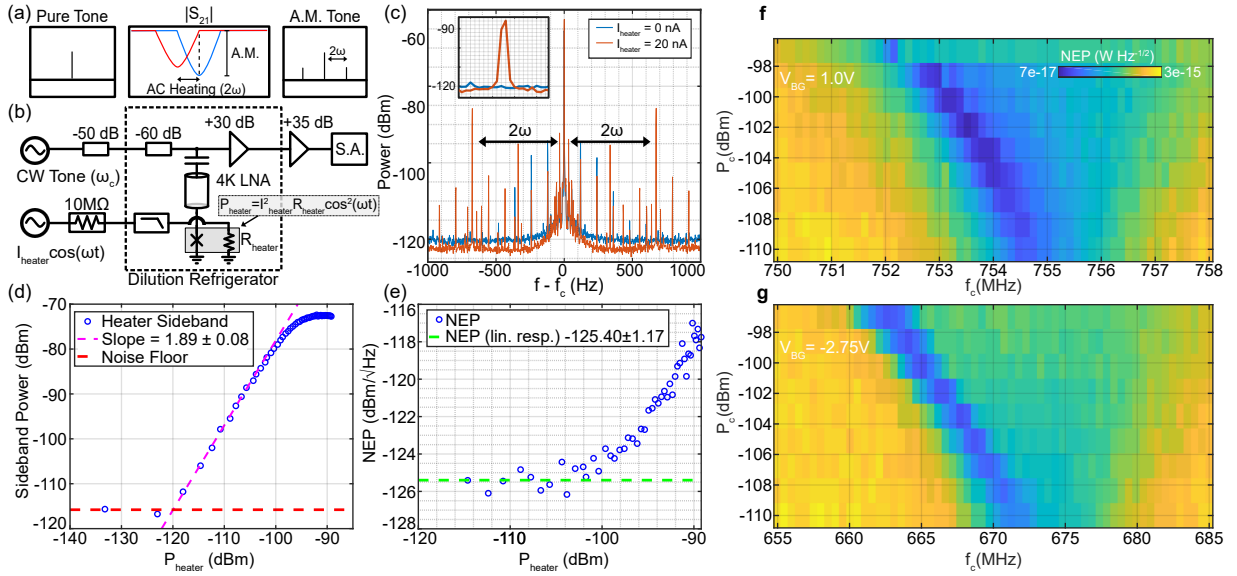


FIG. 9. Noise Equivalent Power (NEP) characterization. (a) Schematic of Measurement Chain. First panel shows a pure carrier tone sent down the microwave line. Second panel shows that an applied ω heater current and subsequent 2ω modulation of the heat power of the graphene flake) yields a 2ω modulation of the transmission function (S_{21} parameter) between unheated (blue) and heated (red) states. The pure tone (dashed line) is placed within the bandwidth of the transmission function and amplitude modulated at 2ω with a modulation index that depends on the magnitude of the S_{21} dip. Third panel shows the amplitude-modulated signal with sidebands at 2ω as it appears on the spectrum analyzer. The measured signal-to-noise ratio of the sideband is used to determine the NEP . (b) Circuit Diagram. A continuous-wave carrier tone at ω_c is sent down a microwave line to the graphene device, amplified, and read out by a spectrum analyzer. An AC heater current at frequency $\omega = 2\pi \times 337$ Hz injects a 2ω heat power P_{heater} in the graphene flake and produces 2ω amplitude modulation of the carrier tone, as discussed in (a). (c) Representative spectrum at output of measurement chain. Spectrum as read out by spectrum analyzer (RBW = 1 Hz) for applied heat power off (blue) and on (red). The primary effect of the applied heat is to produce sidebands spaced at 2ω from the the carrier tone. Other peaks in the spectrum exist at multiples of the line frequency. A peak at ω is consistent with a DC offset in the applied heat power. Inset shows the 2ω sideband. (d) Sideband Power vs. P_{heater} . In the low- P_{heater} linear-response regime, the sideband voltage $V_{sb} \propto P_{heater}$. Since the spectrum analyzer reads out the sideband power, $P_{sb} \propto P_{heater}^2$, which is consistent with the slope at low P_{heater} . (e) NEP vs. P_{heater} . The linear-response regime is characterized by a regime of constant NEP , before rising as the amplitude modulation saturates to its maximal value. The NEP plotted in (g,f) corresponds to the linear response regime (green dashed line). (f, g) NEP vs. carrier power P_c and carrier frequency f_c for (f) electron-side ($V_{BG} = 1.0$ V) and (g) hole-side ($V_{BG} = -2.75$ V). Minimal NEP occurs near the resonance dip minimum where amplitude modulation is largest. As carrier power P_c is increased, the resonance dip downshifts to lower frequencies and is driven into nonlinearity, as characterized by an asymmetric resonance lineshape with steep falling edge and shallow rising edge. The minimum NEP tracks the steep falling edge where amplitude modulation is greatest.

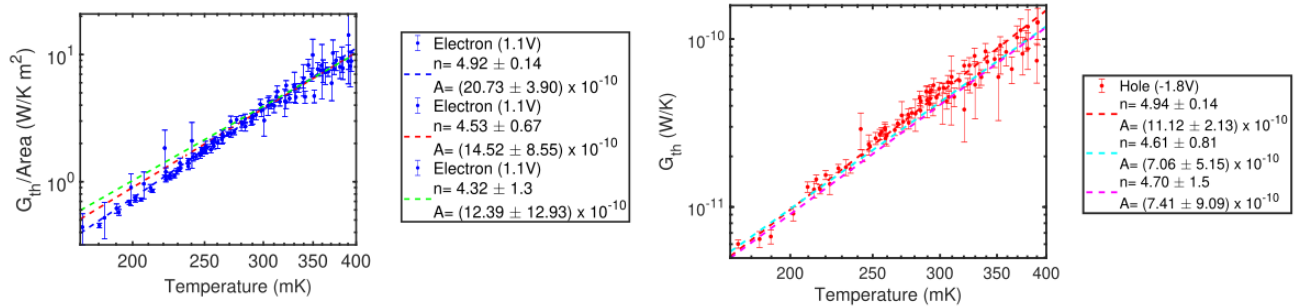


FIG. 10. The fits for the electron and hole doping in different temperature ranges. Electron doping: Blue dashed line is the original full fit from 180 mK to 400 mK. Red is 300 mK to 400mK. Green is 330 mK to 400 mK. Hole doping: Red dashed line is the full data fit. Cyan is 300 mK-390 mK. Magenta is 330 mK-390 mK. For both electron and hole doping the n decreases (but stays well above $n \approx 4$) when part of the data is used for fitting. This indicates that $n = 4$ or $n = 3$ power exponents are inadequate to describe our data.

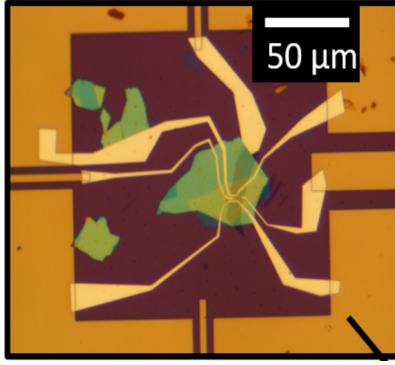


FIG. 11. The optical image showing the area covered in Aluminum and NbTiN. Considering that Al thickness is 100nm the total volume of Aluminum part is $V = 1.5 \times 10^{-16} \text{ m}^3$ approximately. This small Al volume limits the amount of thermalization that can be achieved through contacts.

$$\delta V_{out} \approx \left(\frac{\partial V_{out}}{\partial P_{in}} \Big|_{\delta P_{in}=0} \right) * \delta P_{in}$$

In this regime, the NEP of a power-to-voltage detector (in units of $\frac{W}{\sqrt{Hz}}$) can be defined as that power spectral density at the device input which produces the measured voltage spectral density $\sqrt{S_V}$ at the output:

$$NEP \equiv \frac{\sqrt{S_V}}{\partial V_{out} / \partial P_{heater} |_{\delta P_{heater}=0}}$$

The above expression suggests two immediate ways to measure the NEP . One is to measure the voltage spectral density $\sqrt{S_V}$ at the output and the device responsivity $\partial V_{out} / \partial P_{heater}$. Another is to measure the applied power at the input δP_{in} , and the SNR at the output as suggested by rearranging the above expression

$$NEP \equiv \frac{\sqrt{S_V}}{\delta V_{out}} * \delta P_{in} = \frac{\delta P_{in}}{SNR} = \frac{\delta P_{heater}}{4 \times SNR}$$

In the above equation, the SNR is in units of $\frac{V}{V/\sqrt{Hz}}$ and $P_{in} = P_{heater}/4$. The latter expression is true since we have implicitly assumed P_{in} is that input power that produces the measurable V_{out} signal. In our case, only one quarter of the heat power P_{heater} injected at the heater port produces the measured sideband signal.

2. Experimental Design

To measure the NEP , we use the measurement setup in Fig. 9(a,b) and perform the following procedure:

- We apply a carrier tone on the microwave line (Fig. 9(a), first panel). The S_{21} parameter is the transfer function which determines the magnitude

and phase of the signal at the output. Thus, a carrier tone at the resonant frequency, i.e., at the maximal dip of the S_{21} parameter will have a smaller transmitted magnitude than a carrier tone placed off-resonance.

- Measurement of $P_{heater}(\omega) = I_{heater}(\omega) \times V_{heater}(\omega)$ is achieved by sourcing a current $I_{heater}(\omega)$ to the heater port and measuring the voltage drop $V_{heater}(\omega) = I_{heater}(\omega)R_{heater}$ over the heater port in a 4-wire lock-in measurement. Since we apply an AC heater current $I_{heater}(\omega) \propto \cos \omega t$, it follows that $P_{heater}(\omega) \propto \cos^2 \omega t = \frac{1}{2}(1 + \cos(2\omega t))$. Only the 2ω term in the final expression contributes to the V_{out} sideband signal.
- Applying an AC heat power P_{heater} to the heater port modulates the S_{21} parameter between unheated and heated states (Fig. 9(a), second panel). Consistent with the heating measurements performed in the main text, the heated state has a lower resonant frequency and lower quality factor than the unheated state. The 2ω component of the input power P_{heater} modulates the flake temperature at 2ω . Thus, modulation of the S_{21} resonance feature will occur at 2ω .
- Placing the frequency of the carrier tone within the bandwidth of the modulated S_{21} resonance feature will amplitude modulate the carrier, producing sidebands spaced at 2ω from the carrier (Fig. 9(a), second and third panel). Provided that the device is in the linear-response regime, the voltage of the sidebands will increase in proportion to applied heat power, i.e. $V_{sb} \propto P_{heater}$. It follows that the power of the sidebands will increase as $P_{sb} \propto P_{heater}^2$.
- The amplitude-modulated carrier is read out by a spectrum analyzer (Fig. 9(a), third panel). The signal-to-noise ratio of the sideband is used to calculate the NEP . We note that only one sideband

is used in the NEP measurement.

3. Sideband Spectrum

In Fig. 9(c), we see that application of an AC heater current of magnitude $I_{heater} = 20$ nA results in sidebands at 2ω offset from the carrier, where $\omega = 2\pi \times 337$ Hz. In addition to the 2ω sidebands, sidebands at multiples of the 60 Hz line frequency frequency are present. Additionally, there are sidebands at ω approximately 10 dB down from the 2ω sidebands. This can be explained by a small DC offset in the heater current.

With increasing heater power, the magnitude of the sidebands saturates at a value consistent with expectations. It is straightforward to show that a resonance dip of 3 dB generates a maximum amplitude modulation index $m = 17\%$, which should produce sidebands 21 dB lower than the carrier. This is in agreement with the measured sideband magnitude that is 23 dB lower than the carrier.

4. Sideband Scaling

In the linear response regime, $V_{sb} \propto \delta P_{heater}$. Therefore, the sideband signal as measured on the spectrum analyzer (in power units) should scale as $P_{sb} \propto P_{heater}^2$, or by 20 dB/decade. This is seen in Fig. 9(d) for applied heat P_{heater} in the range -120 dBm to -105 dBm, where the slope of fit at low- P_{heater} is consistent with a scaling exponent $n = 2$. This confirms that our measurement is in linear-response regime at low P_{heater} . For greater applied P_{heater} , the sideband power saturates as the amplitude modulation reaches the full maximum of the resonance dip.

5. NEP vs. P_{heater}

In the linear response regime, the NEP is constant with respect to P_{heater} since $V_{sb} \propto P_{heater}$. This is shown Fig. 9e for $P_{heater} < -105$ dBm. As stated above, the NEP rises for $P_{heater} > -105$ dBm as the SNR saturates while P_{heater} continues to increase.

6. NEP vs. Carrier Frequency and Carrier Power

To explore the NEP as a function of the carrier tone, we generate a heat map with swept carrier frequency f_c and carrier power P_c (Fig. 9(f,g)). For the lowest carrier powers, the NEP is minimized for carrier frequencies close to the resonance minimum, where the responsivity of the resonance to applied heater power is greatest and therefore the amplitude modulation of the carrier is greatest. As the carrier power P_c is increased, the junction is driven to nonlinearity, resulting in a resonance dip with a steep falling edge and a shallow rising edge. This has the effect of enhancing the NEP on the falling edge and reducing it on the rising edge. For carrier powers $P_c > -98$ dBm, the quality factor of the resonance feature is degraded to such an extent that the amplitude modulation of sideband is reduced and the NEP increases. The NEP reaches a minimum value of 7×10^{-17} W/ $\sqrt{\text{Hz}}$ for a carrier power $P_{carrier} = -102$ dBm and carrier frequency $f_{carrier} = 753.5$ MHz.

7. Detection Limits

The measured minimum noise-equivalent power $NEP_{min} \approx 7 \times 10^{-17}$ W/ $\sqrt{\text{Hz}}$. It is limited by the noise of the 4K cryoamp and is $\sim 20\times$ larger than the thermal fluctuation-limited $NEP = \sqrt{4k_B T^2 G_{th}}$ at $T_{mxc} = 200$ mK. At $T_{mxc} = 58$ mK, the projected thermal fluctuation-limited $NEP_{proj} \approx 1 \times 10^{-19}$ W/ $\sqrt{\text{Hz}}$, assuming that the T^4 dependence of G_{th} holds down to these temperatures [29, 38]. The corresponding thermal fluctuation-limited energy resolution $\delta E = NEP_{proj} \sqrt{\tau_{th}} \approx h \times 65$ GHz, assuming the projected thermal time constant $\tau_{th} = \frac{C_{th}}{G_{th}} \approx 170$ ns, $n_{carrier} = \frac{10^{12}}{\text{cm}^2}$, $A = 25 \mu\text{m}^2$.

-
- [1] Fong, K. C. & Schwab, K. C. Ultrasensitive and Wide-Bandwidth Thermal Measurements of Graphene at Low Temperatures. *Physical Review X* **2**, 031006 (2012).
 [2] Fong, K. C. *et al.* Measurement of the Electronic Thermal Conductance Channels and Heat Capacity of Graphene at Low Temperature. *Physical Review X* **3**, 041008 (2013).
 [3] Borzenets, I. V. *et al.* Ballistic Graphene Josephson Junctions from the Short to the Long Junction Regimes. *Phys-*

- ical Review Letters* **117**, 237002 (2016).
 [4] Calado, V. E. *et al.* Ballistic Josephson junctions in edge-contacted graphene. *Nature Nanotechnology* **10**, 761–764 (2015).
 [5] Draelos, A. W. *et al.* Supercurrent Flow in Multiterminal Graphene Josephson Junctions. *Nano Letters* **19**, 1039–1043 (2019).
 [6] Schmidt, F. E., Jenkins, M. D., Watanabe, K., Taniguchi, T. & Steele, G. A. A ballistic graphene superconduct-

- ing microwave circuit. *Nature Communications* **9**, 4069 (2018).
- [7] Borzenets, I. V. *et al.* Phonon Bottleneck in Graphene-Based Josephson Junctions at Millikelvin Temperatures. *Physical Review Letters* **111**, 027001 (2013).
- [8] Lee, G.-H. *et al.* Graphene-based Josephson junction microwave bolometer. *Nature* **586**, 42–46 (2020).
- [9] Halbertal, D. *et al.* Imaging resonant dissipation from individual atomic defects in graphene. *Science* **358**, 1303–1306 (2017).
- [10] Saira, O.-P., Zgirski, M., Viisanen, K. L., Golubev, D. S. & Pekola, J. P. Dispersive Thermometry with a Josephson Junction Coupled to a Resonator. *Physical Review Applied* **6**, 024005 (2016).
- [11] Kong, J. F., Levitov, L., Halbertal, D. & Zeldov, E. Resonant electron-lattice cooling in graphene. *Physical Review B* **97**, 245416 (2018).
- [12] Tikhonov, K. S., Gornyi, I. V., Kachorovskii, V. Y. & Mirlin, A. D. Resonant supercollisions and electron-phonon heat transfer in graphene. *Physical Review B* **97**, 085415 (2018).
- [13] Wang, J. I.-J. *et al.* Coherent control of a hybrid superconducting circuit made with graphene-based van der Waals heterostructures. *Nature Nanotechnology* **14**, 120–125 (2019).
- [14] Tinkham, M. *Introduction to Superconductivity* (Publisher: Dover Publications, 2004).
- [15] Viljas, J. K. & Heikkilä, T. T. Electron-phonon heat transfer in monolayer and bilayer graphene. *Physical Review B* **81**, 245404 (2010).
- [16] Chen, W. & Clerk, A. A. Electron-phonon mediated heat flow in disordered graphene. *Physical Review B* **86**, 125443 (2012).
- [17] Roukes, M. L., Freeman, M. R., Germain, R. S., Richardson, R. C. & Ketchen, M. B. Hot electrons and energy transport in metals at millikelvin temperatures. *Physical Review Letters* **55**, 422–425 (1985).
- [18] Halbertal, D. *et al.* Nanoscale thermal imaging of dissipation in quantum systems. *Nature* **539**, 407–410 (2016).
- [19] Kokkonen, R. *et al.* Bolometer operating at the threshold for circuit quantum electrodynamics. *Nature* **586**, 47–51 (2020).
- [20] Day, P. K., LeDuc, H. G., Mazin, B. A., Vayonakis, A. & Zmuidzinas, J. A broadband superconducting detector suitable for use in large arrays. *Nature* **425**, 817–821 (2003).
- [21] Wandui, A. *et al.* Thermal kinetic inductance detectors for millimeter-wave detection. *Journal of Applied Physics* **128**, 044508 (2020).
- [22] Walsh, E. D. *et al.* Graphene-Based Josephson-Junction Single-Photon Detector. *Physical Review Applied* **8**, 024022 (2017).
- [23] Lara-Avila, S. *et al.* Towards quantum-limited coherent detection of terahertz waves in charge-neutral graphene. *Nature Astronomy* **3**, 983–988 (2019).
- [24] Hochberg, Y., Kahn, Y., Lisanti, M., Tully, C. G. & Zurek, K. M. Directional detection of dark matter with two-dimensional targets. *Physics Letters B* **772**, 239–246 (2017).
- [25] Kim, D., Park, J.-C., Fong, K. C. & Lee, G.-H. Detecting keV-Range Super-Light Dark Matter Using Graphene Josephson Junction. *arXiv:2002.07821 [cond-mat, physics:hep-ex, physics:hep-ph]* (2020). 2002.07821.
- [26] McAllister, B. T. *et al.* The ORGAN experiment: An axion haloscope above 15 GHz. *Physics of the Dark Universe* **18**, 67–72 (2017).
- [27] Baracchini, E. *et al.* PTOLEMY: A Proposal for Thermal Relic Detection of Massive Neutrinos and Directional Detection of MeV Dark Matter. *arXiv:1808.01892 [astro-ph, physics:hep-ex, physics:physics]* (2018). 1808.01892.
- [28] Roukes, M. L. Yoctocalorimetry: Phonon counting in nanostructures. *Physica B: Condensed Matter* **263–264**, 1–15 (1999).
- [29] Mather, J. C. Bolometer noise: Nonequilibrium theory. *Applied Optics* **21**, 1125–1129 (1982).
- [30] Geerlings, K. *et al.* Improving the quality factor of microwave compact resonators by optimizing their geometrical parameters. *Applied Physics Letters* **100**, 192601 (2012).
- [31] M. Pozar, D. *Microwave Engineering, 4th Edition* (Wiley, 2011).
- [32] Van Duzer, T. & W Turner, C. *Principles of Superconductive Devices and Circuits* (Pearson, 1998).
- [33] Lee, G.-H., Kim, S., Jhi, S.-H. & Lee, H.-J. Ultimately short ballistic vertical graphene Josephson junctions. *Nature Communications* **6**, 6181 (2015).
- [34] Nanda, G. *et al.* Current-Phase Relation of Ballistic Graphene Josephson Junctions. *Nano Letters* **17**, 3396–3401 (2017).
- [35] Voutilainen, J. *et al.* Energy relaxation in graphene and its measurement with supercurrent. *Physical Review B* **84**, 045419 (2011).
- [36] Giazotto, F., Heikkilä, T. T., Luukanen, A., Savin, A. M. & Pekola, J. P. Opportunities for mesoscopics in thermometry and refrigeration: Physics and applications. *Reviews of Modern Physics* **78**, 217–274 (2006).
- [37] Timofeev, A. V. *et al.* Recombination-Limited Energy Relaxation in a Bardeen-Cooper-Schrieffer Superconductor. *Physical Review Letters* **102**, 017003 (2009).
- [38] Moseley, S. H., Mather, J. C. & McCammon, D. Thermal detectors as x-ray spectrometers. *Journal of Applied Physics* **56**, 1257–1262 (1984).